Nonlinear Dyn (2024) 112:8811–8830
https://doi.org/10.1007/s11071-024-09505-y

ORIGINAL PAPER

Finding an optimal shape of a curved mechanical beam for enhanced internal resonance

Sahar Rosenberg · Yuri Feldman · Oriel Shoshani

Received: 22 September 2023 / Accepted: 11 February 2024 / Published online: 16 April 2024

Abstract One of the most interesting nonlinear phenomena of mode coupling is internal resonances, which can promote directed energy transfer from one eigenmode to another, even at small amplitudes in free or forced oscillations. Internal resonances can be highly beneficial for many engineering applications. However, in most cases, internal resonances are encountered either accidentally or by proper tuning of different control parameters during experiments without prior planning. Therefore, the ability to a priori design a mechanical resonator with intentional internal resonance at given amplitudes holds great promise. Here, we show a simple methodological way to manipulate the eigenfrequencies and the coupling between the eigenmodes of a doubly clamped mechanical beam using a genetic algorithm for shape optimization of the initial curvature of the beam. We demonstrate that our methodology can be applied to both 1-to-2 and 1-to-3 internal resonances of micro-beams. Our results pave the way to a new class of design techniques for internal resonance enhancement based on shape optimization.

S. Rosenberg (✉) · Y. Feldman · O. Shoshani
Ben-Gurion University of the Negev, 84105 Beer-Sheva, Israel
e-mail: saharros@post.bgu.ac.il

Y. Feldman
e-mail: yurifeld@bgu.ac.il

O. Shoshani
e-mail: oriels@bgu.ac.il

Keywords Internal resonance · Shape optimization · Genetic algorithm · Curved mechanical beam

1 Introduction

In contrast to the well-understood dynamics of linear systems, nonlinear systems are significantly more challenging, e.g., small fluctuations can lead to large responses, and there is a plethora of phenomena that cannot be found in linear systems, such as isolated limit cycles, multiple co-existing solutions, energy-dependent frequency, bifurcations, and chaos [1,2]. However, the complexity of nonlinear systems does not necessarily limit their performance. In fact, there are several applications where nonlinearity can serve as a means to improve the performance of engineering applications. Examples include mechanical amplification schemes [3], improved frequency stability [4,5], increased dynamic range [6–8], and noise suppression procedures [9,10]. Consequently, the ability to manipulate the nonlinearity in resonators allows one to design devices with greater control over their dynamical responses [11]. One way to manipulate the nonlinearities of a resonator is by using shape optimization methods, where changing the cross-sectional area of a resonator or its shape function causes a decrease/increase in the geometric contribution to the resonator nonlinearities [12,13]. More sophisticated methods, such as topology optimization, which does not require a baseline design, and the central task is to determine which

geometric points in the design mesh should be material points and which points should contain no material [14], and materials optimization and meta-materials, which also allow greater control on the properties of the device [15], can also be used.

Mode coupling has recently become the focus of many studies [16–18], which explore previously unknown phenomena and new applications for their use to improve resonator performance. The mode coupling of mechanical resonators has been commonly used in the design of MEMS filters [19,20], inertial sensors [21,22], and mass sensing [23,24]. Perhaps, the most interesting phenomenon of mode coupling is internal resonance (IR) in which eigenfrequencies are (exactly or nearly) rationally related. That is, $\omega_1/\omega_2 \approx n/m$ where n and m are integers, constitutes the so-called n-to-m IR [25]. IRs may be activated in free as well as forced oscillations and are responsible for the redistribution of energy between the interacting eigenmodes of the system. The IRs promote directed or targeted energy transfer from one eigenmode of a dynamical system to another, even for small (weakly nonlinear) amplitudes [26–28] and are most prominent in systems with small dissipation, such as micro- and nano-resonators [29–32]. Nevertheless, IRs have also been thoroughly explored in the macro-scale mechanical systems; examples include the studies of Miles [33,34] and Johnson and Bajaj [35] for the 1-to-1 IR, Sethna [36] and Haddow et al. [37] for the 1-to-2 IR, Chin and Nayfeh [38,39] for the 1-to-3 IR, and at least two monographs entirely devoted to the subject [25,40]. The IRs can be highly beneficial for many engineering applications, such as phase-noise suppression [4], frequency-combs generation [41,42], tunable damping and relaxation rates [43,44], and enhanced energy harvesting [45,46].

To date, most IRs are encountered either accidentally or by "on the fly" proper tuning of different control parameters [47,48]. Therefore, the ability to predesign a mechanical resonator with targeted IR that occurs at predetermined amplitudes holds great promise. In this paper, we consider, perhaps, the simplest way to achieve this goal. Specifically, we present a means of manipulating the eigenfrequencies and the coupling between the eigenmodes of a doubly clamped mechanical beam using a genetic algorithm for shape optimization of the initial curvature of the beam (which is significantly simpler than other optimization methods). We show that the genetic algorithm chooses the optimal initial shape of a curved beam to alter the conservative nonlinearities and achieve 1-to-3 and 1-to-2 IRs. The rest of the paper is organized as follows: in Sect. 2, we derive the governing equations for two-mode internal resonance from the nonlinear partial integrodifferential equation of the curved beam using Galerkin projection; in Sect. 3, we present the methods used for the shape optimization and the procedure to obtain the final design of the beams; in Sect. 4, we illustrate the application of our methodology to MEMS devices with specified physical properties and validate our final designs by comparing numerically obtained dynamic responses with the corresponding analytically calculated resonant envelope modulations. Section 5 summarizes our main findings and discusses their implications.

2 Problem formulation

We consider the conservative transverse vibration of a clamped-clamped shallow arch mechanical beam with a shape described by the function $w_0(x)$, width b, thickness d and length ℓ (Fig. 1). The beam is idealized as a one-dimensional element, where the transverse displacement field $w(x,t)$ is planar along the z axis, and perpendicular to the axis of the beam, x. The beam has constant density ρ, Young's modulus $\mathcal{E}$, and cross-section $A = b \times d$. Using the Euler-Bernoulli beam model, the nonlinear (truncated at cubic order) equation governing the transverse motion of the beam is given by[1] [49–53]

$$\mathcal{E}I\frac{\partial^4\tilde{w}}{\partial\tilde{x}^4} + \rho A\frac{\partial^2\tilde{w}}{\partial\tilde{t}^2} - \frac{\mathcal{E}A}{2\ell}\left[\frac{\partial^2\tilde{w}}{\partial\tilde{x}^2} - \frac{\partial^2\tilde{w}_0}{\partial\tilde{x}^2}\right] \int_0^\ell \left[\left(\frac{\partial\tilde{w}}{\partial\tilde{x}}\right)^2 - 2\left(\frac{\partial\tilde{w}}{\partial\tilde{x}}\frac{\partial\tilde{w}_0}{\partial\tilde{x}}\right)\right] d\tilde{x} = 0, \tag{1}$$

and subject to the clamped-clamped boundary conditions

$$\tilde{w}(0,\tilde{t}) = \tilde{w}(\ell,\tilde{t}) = \frac{\partial\tilde{w}}{\partial\tilde{x}}(0,\tilde{t}) = \frac{\partial\tilde{w}}{\partial\tilde{x}}(\ell,\tilde{t}) = 0. \tag{2}$$

Rescaling the spatial variables by ℓ ($x = \tilde{x}/\ell, w = \tilde{w}/\ell, w_0 = \tilde{w}_0/\ell$) and time by $t = \tilde{t}\sqrt{\mathcal{E}I/\rho A\ell^4}$, we

[1] Under the assumption of a shallow arch, where terms of order $O(\tilde{w_0}^n)$ with $n > 1$, and their derivatives, can be neglected.

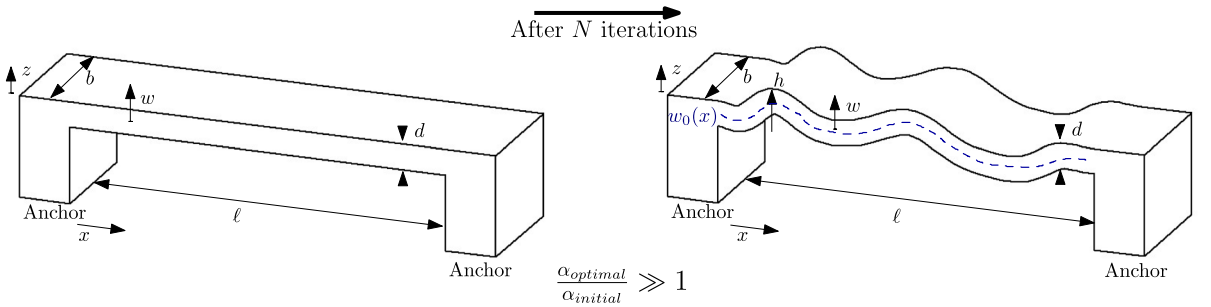

Fig. 1 Shape optimization of a curved mechanical beam. The doubly clamped beam of length ℓ and rectangular cross-section ($b \times d$) is straight in the initial configuration (left panel). The curvature of the beam is modified in each iteration by the genetic algorithm via the function $w_0(x)$ (the blue dashed line), which is confined to a maximal depth h. The final configuration of the curved beam is retrieved after N iterations (right panel) and exhibits IR relation between its first two modes and enhanced mode coupling, where α is the coupling strength. (Color figure online)

obtain the following non-dimensional partial integro-differential equation

$$\ddot{w} + w^{IV} - \chi\left(w'' - w_0''\right) \int_0^1 \left(\left(w'\right)^2 - 2\left(w'w_0'\right)\right) dx = 0, \tag{3}$$

where the dot overhead symbol denotes differentiation with respect to the non-dimensional time, the prime symbol denotes differentiation with respect to the non-dimensional axial direction x, the "IV" superscript denotes the fourth derivative with respect to the non-dimensional axial direction x, and $\chi = 6(\ell/d)^2$ is the aspect ratio parameter. We assume that the motion of the beam is dominated by its first two modes, $w(x,t) = \phi_1(x)q_1(t) + \phi_2(x)q_2(t)$, and perform a Galerkin projection (Appendix A) of Eq. (3) onto $\phi_1(x)$ and $\phi_2(x)$ to obtain a pair of nonlinearly coupled ordinary differential equations of the modal coordinate $q_1(t)$ and $q_2(t)$

$$\ddot{q}_1 + \omega_1^2 q_1 + c_{(2,0)}q_1^2 + c_{(1,1)}q_1q_2 + c_{(0,2)}q_2^2 + c_{(3,0)}q_1^3 + c_{(2,1)}q_1^2q_2 + c_{(1,2)}q_1q_2^2 + c_{(0,3)}q_2^3 = 0, \tag{4}$$

$$\ddot{q}_2 + \omega_2^2 q_2 + d_{(2,0)}q_1^2 + d_{(1,1)}q_1q_2 + d_{(0,2)}q_2^2 + d_{(3,0)}q_1^3 + d_{(2,1)}q_1^2q_2 + d_{(1,2)}q_1q_2^2 + d_{(0,3)}q_2^3 = 0. \tag{5}$$

The indices in the parenthesis of the coefficients $c_{(i,j)}$ and $d_{(i,j)}$ indicate the power i of the modal coordinate q_1 and the power j of the modal coordinate q_2. For a given IR, many of the nonlinear terms that couple the modal coordinates in Eqs. (4)–(5) can be disregarded as they do not promote energy exchange between the modes, and therefore, have negligible effects on the system dynamics. There are several systematic ways to eliminate these non-resonant terms, such as the method of averaging, multiple scales, and normal forms [54–57]. However, we are focusing only on 1-to-2 and 1-to-3 IRs, which are associated with a single-term coupling potential $U_{\text{cpl}} = \alpha q_1^n q_2$, where $n = 2$ for the 1-to-2 IR [43] and $n = 3$ for the 1-to-3 IR [58]. Hence, we can rewrite Eqs. (4)-(5) in the following compact form

$$\ddot{q}_1 + \omega_1^2 q_1 + n\alpha q_1^{n-1} q_2 + \beta_1 q_1^2 + \gamma_1 q_1^3 = 0, \tag{6}$$

$$\ddot{q}_2 + \omega_2^2 q_2 + \alpha q_1^n + \beta_2 q_2^2 + \gamma_2 q_2^3 = 0, \tag{7}$$

where there is a single coupling term[2] in each model equation with a single coupling coefficient (α), and there are two additional nonlinear terms, quadratic ($\beta_{1,2}$) and cubic ($\gamma_{1,2}$) that belong to the isolated dynamics of each mode, i.e., not related to the modal interaction. All of these coefficients are either directly or indirectly (via the eigenmodes) depend on the initial shape of the beam. As described in detail in the next section, we use a genetic algorithm [59] to find the optimal shape of the beam $w_0(x)$ to reach IR conditions while enhancing the coupling α between the modes.

[2] We omitted here the dispersive coupling terms that stem from the potential $U_{\text{dpr}} = \eta q_1^2 q_2^2$, which do not promote energy exchange in 1-to-2 and 1-to-3 IRs [58].

3 Methodology and procedures

In this section, we present the methods that we used for the shape optimization procedure and our way of systematically applying the genetic algorithm with numerical methods to optimize the geometric nonlinearities of the beam for 1-to-2 and 1-to-3 IRs.

3.1 Numerical methods

In all the numerical calculations in this paper, we use the spectral method for the spatial discretization on Chebyshev grid $x_j = \cos(j\pi/J), \quad j = 0, 1, ..., J$, where $J+1$ is the number of grid points. For the smooth functions that we consider in this study, spectral methods provide considerably higher accuracy for differentiation and integration over other numerical methods, such as finite differences, and finite elements [60]. We use the Chebyshev differentiation matrices [61,62], which are calculated on a Chebyshev grid that clusters at the boundaries. This allows us to accurately describe the function by interpolating polynomials over the entire computational domain using a relatively small number of basis functions. The numerical integration on the Chebyshev points is done by using the Clenshaw-Curtis quadrature [61], which is defined by integrating the polynomial interpolant. For the time stepping, we use the ODE45 solver of Matlab, which is based on a six-stage, fifth-order, Runge-Kutta method. Due to the fast convergence of the spectral method, we use a time step of order $\mathcal{O}(\Delta t) = 10 \cdot J^{-3}$, which yields a stable numerical scheme for all the simulations that we conducted (see Sect. 4 for discussion on numerical stability).

3.2 Eigenmodes of a curved beam

To find the eigenmodes for the Galerkin projection, we assume a modal solution of the form $w(x,t) = \phi(x)\exp(i\omega t)$ and obtain (after integration by parts and applying boundary conditions) from the linear part of Eq. (3) the following boundary value problem

$$\phi^{IV} - 2\chi w_0'' \int_0^1 \phi w_0'' dx = \omega^2 \phi, \quad \phi = \phi' = 0 \ \ @x = 0, 1. \tag{8}$$

We numerically solve Eq. (8) by using the Chebyshev differentiation matrices and the Clenshaw-Curtis quadrature weights [61]. To assess the validity of the numerical eigenmodes solver, we test it on a curved beam with an initial shape $w_0(x) = h[\cosh(4.73x) - \cos(4.73x) - 0.98(\sinh(4.73x) - \sin(4.73x))]$. We note that the chosen shape, w_0, is identical to the first mode of a doubly clamped straight beam with a prefactor $h \ll 1$ (see Fig. 2). Thus, for sufficiently small h, the integral term in Eq. (8) tends to zero (both from the orthogonality of the eigenmodes and the smallness of w_0) and we recover the eigenmodes of a straight beam $\phi_k = C_k[\cosh(\lambda_k x) - \cos(\lambda_k x) - \alpha_k(\sinh(\lambda_k x) - \sin(\lambda_k x))]$, where $\lambda_k = \{4.7300, 7.8532, 10.9956, 14.1372, ...\}$, $\alpha_k = (\cosh\lambda_k - \cos\lambda_k)/(\sinh\lambda_k - \sin\lambda_k)$, and the constant C_k satisfy the orthonormality condition: $\langle\phi_k, \phi_l\rangle = \int_0^1 \phi_k\phi_l dx = \delta_{kl}$.

3.3 Frequency crossing of the isolated modes

To ensure a resonant interaction between the first and second modes of the beam, it is desired to engineer these modes such that the weighted energy-dependent frequencies ($\Omega_{1,2}$) of the isolated modes (i.e., when $\alpha = 0$) will intersect at a non-zero energy level $n\Omega_1(E_1) - \Omega_2(E_2) = 0$, $n = 2, 3$, $E_1 + E_2 \neq 0$. When this frequency crossing condition is satisfied, we can prepare the individual modes with the prescribed energy for frequency crossing (E_1 and E_2, respectively) and observe resonant modal interaction (which is manifested via frequency repulsion/anti-crossing/veering [63,64]) even for low values of the coupling coefficient α.

The equations of motion for the isolated modes are given by $\ddot{q}_i + \omega_i^2 q_i + \beta_i q_i^2 + \gamma_i q_i^3 = 0$, $i = 1, 2$, which can be integrated (due to conservation of energy) to yield $\dot{q}_i^2/2 + U_i(q_i) = E_i$, where $U_i = \omega_i^2 q_i^2/2 + \beta_i q_i^3/3 + \gamma_i q_i^4/4$. Thus, as described in Ref. [53] and in Appendix B, the frequency of oscillation of the isolated mode is given by

$$\Omega_i(E_i) = \frac{\pi}{2K(k_i)}\sqrt{\frac{\gamma}{2} z_i^{(1)} z_i^{(2)}}, \tag{9}$$

where $K(k_i)$ is an elliptic integral of the first kind, $k_i^2 = [(q_i^{(1)} - q_i^{(2)})^2 - (z_i^{(1)} - z_i^{(2)})^2]/(4z_i^{(1)}z_i^{(2)})$, $z_i^{(j)} = [(q_i^{(3)} - q_i^{(j)})(q_i^{(4)} - q_i^{(j)})]^{1/2}$, $j = 1, 2$, and $q_i^{(j)}$ ($j = 1, 2, 3, 4$) are the roots of the quartic equation $U_i(q_i) = E_i$ in which $q_i^{(1)} > q_i^{(2)}$ are the

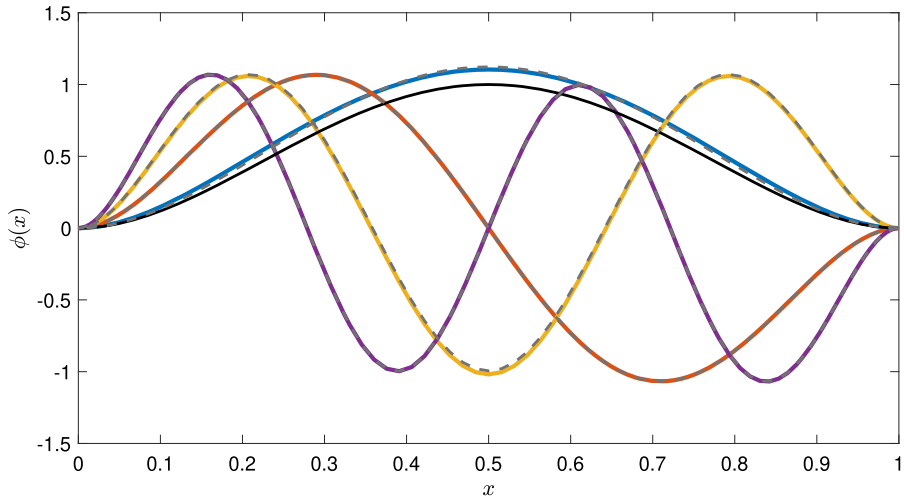

Fig. 2 The normalized first four modes of a doubly clamped beam with an initial shape of the first mode of a straight beam with normalized (by the length of the beam) height of $h = 0.001$ (black). The wavenumber of the first mode (blue) is $\lambda_1 = 5.4061$, for the second mode (in orange) $\lambda_2 = 7.8532$, third mode (yellow) $\lambda_3 = 11.0387$, and the fourth mode (purple) $\lambda = 14.1372$. The gray dashed lines are the modes of the straight beam. (Color figure online)

real and $q_i^{(3)} = q_i^{(4)*}$ are complex conjugates [65]. Equation (9) provides an exact expression for the frequency of oscillation of the isolated mode for any energy level E_i, and therefore, can be used to find modes that satisfy the frequency crossing condition $n\Omega_1(E_1) - \Omega_2(E_2) = 0,\ n = 2, 3,\ E_1 + E_2 \neq 0$ (see Fig. 3).

To prepare the modes in the appropriate energy levels for resonant interaction, we write the expression for the potential energy of the beam [53,66]

$$U = \frac{1}{2}\int_0^1 w''^2 dx + \frac{\chi}{4}\int_0^1 \left(\int_0^1 \left(2w_0' w' - w'^2\right) dx\right)^2 dx. \quad (10)$$

Using our two-mode approximation $w(x,t) = q_1(t)\phi_1(x) + q_2(t)\phi_2(x)$, we find from Eq. (10) that $U = U_1 + U_2 + U_{\text{cpl}}$. Therefore, by initiating the oscillation of the beam from rest $\dot{q}_{1,2}(0) = 0$, we find that the initial deflection of the beam $w(x,0) = \phi_1(x)q_1(0) + \phi_2(x)q_2(0)$ can be calculated from the algebraic equations $U_1 = U(q_1(0)) = E_1$ and $U_2 = U(q_2(0)) = E_2$.

As depicted in Fig. 3, there are two possible options to generate the desired frequency crossing condition for enhanced resonant interaction. In the 1-to-2 IR (left panel), there is a crossing of the backbone curves, which means that there is an energy level $E_1 = E_2 = E_{\text{cross}}$, such that $n\Omega_1(E_{\text{cross}}) - \Omega_2(E_{\text{cross}}) = 0$. This option is possible only if one of the modes experiences a non-monotonic dependence of the oscillation frequency on the energy [53] or if the effective stiffness of one mode is higher than the other while its weighted eigenfrequency is lower, e.g., $n\omega_1 < \omega_2$ and $n\gamma_{\text{eff}_1} > \gamma_{\text{eff}_2}$, where $\gamma_{\text{eff}_{1,2}} = \gamma_{1,2} - (10/9)(\beta_{1,2}/\omega_{1,2})^2$ [67]. In the second option, which is more accessible, we prepare the individual modes at different energy levels $E_1 \neq E_2$ to satisfy the frequency crossing condition. The right panel of Fig. 3 shows such a scenario for the 1-to-3 IR.

3.4 The genetic algorithm

Our genetic algorithm uses an initial shape function of a straight beam $w_{(0,0)} = 0$ to create a population (a group of shape functions) of other solutions in its vicinity (the first index refers to the generation, and the second index refers to the individual in the population). After calculating the coupling coefficient α, the ratio between the eigenfrequencies of the modes ω_2/ω_1, and the condition of frequency crossing at non-zero energy levels (as described in Sect. 3.3), for each individual (a certain shape function) of the population, the algorithm sorts the population by fitness and creates the next gen-

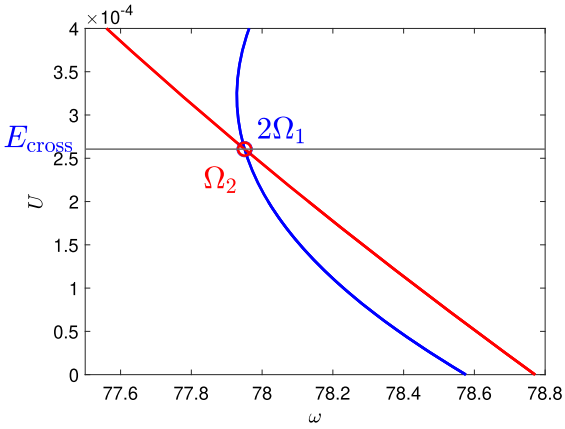

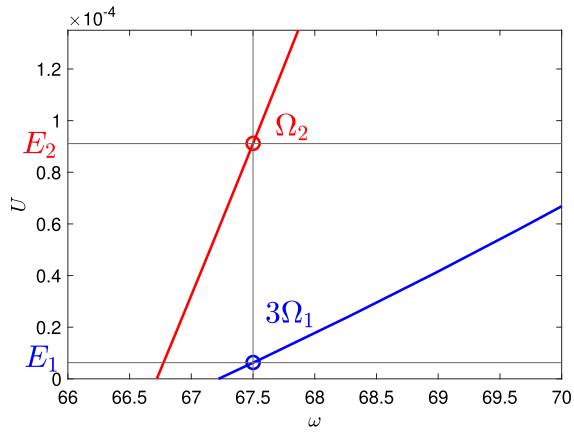

Fig. 3 The energy-frequency backbone curves of the first and second modes for the case of 1-to-2 IR (on the left panel) and the case of 1-to-3 IR (on the right panel). E_1 and E_2 represents the energy levels required for each isolated mode in order to satisfy the frequency crossing condition $n\Omega_1(E_1) - \Omega_2(E_2) = 0,\ n = 2, 3,\ E_1 + E_2 \neq 0$

eration of the population. Mathematically, the genetic algorithm solves the following minimization problem

$$\min_{w_0(x)} \quad [\alpha(w_0(x), \phi_1(w_0(x)), \phi_2(w_0(x))]^{-1} \tag{11a}$$

$$\text{s.t.} \quad w_0(x) = w_0'(x) = 0 \ \ @x = 0, 1 \tag{11b}$$

$$|\omega_2/\omega_1 - 1/n| < \epsilon,\ n = 2, 3,\ \epsilon \ll 1 \tag{11c}$$

$$n\Omega_1(E_1) - \Omega_2(E_2) = 0,\ n = 2, 3,$$
$$E_1 + E_2 \neq 0. \tag{11d}$$

To this end, we use the following three operators:***(i) Transcendence operator*** in which the fittest solutions survive for the next generation, i.e., $w_{(t+1,i)} = w_{(t,i)}$. Here, the fittest solutions will be the ones that provide a ratio between the natural frequencies ω_2/ω_1, which is closer to IR ratio than the rest, and the coupling coefficient α is larger than the rest, while also ensuring that the frequencies of the isolated modes intersect at a non-zero energy level. Since there could be multiple solutions for the genetic algorithm, it is designed so that the ratio of the natural frequencies of the fittest shape functions will lie within a certain range of the IR and the fittest solution will have the highest coupling between the modes (for more details in a specific case, see Sect. 4). ***(ii) Crossover operator***, where each pair of solutions is being used to create a new solution. For continuity of the new shape function, we use a random number $r_1 \in [0, 1]$ (using "rand" function in Matlab which returns a random scalar from the uniformly distributed interval) to be the weight of each "parent" in creating the "child" solution, i.e., $w_{(t+1,i)} = r_1 \cdot w_{(t,i)} + (1 - r_1) \cdot w_{(t,i+1)}$. And, ***(iii) Mutation operator***, where the solutions are changed by adding a random order Chebyshev polynomial multiplied by a second polynomial that satisfies the boundary conditions, i.e., $w_{(t+1,i)} = w_{(t,i)} + T_k(x) \cdot r_2 \cdot P_{BC}$, where $T_k(x)$ is the k-th Chebyshev polynomial of the first kind with $k > 1$ [68], r_2 is a random number from the uniformly distributed interval $r_2 \in [-1, 1]$, and $P_{BC} = 16x^2(x - 1)^2$ is a polynomial that enforce the boundary conditions with a maximal value of 1 at the midpoint of the beam $x = 1/2$.

The probability of these operators is defined in advance by the percentage of the next generation population that is created by each of them. The algorithm finds an optimal shape that enhances the coupling coefficient α, while satisfying $|\omega_1/\omega_2 - 1/n| < \epsilon,\ \epsilon \ll 1,\ n = 2, 3$, and ensuring a frequency crossing at a non-zero energy level. A summary of the shape optimization procedure is depicted in the flow chart below (Fig. 4).

4 Analysis and design of beams with enhanced IRs

For an illustration of our methodology, we use a microbeam with physical dimensions of $\ell = 1000\mu$m, $d = 2\mu$m, $b = 30\mu$m (which yield $A = b \cdot d = 60\mu\text{m}^2$, and $I = b \cdot d^3/12 = 20\mu\text{m}^4$), and mechanical prop-

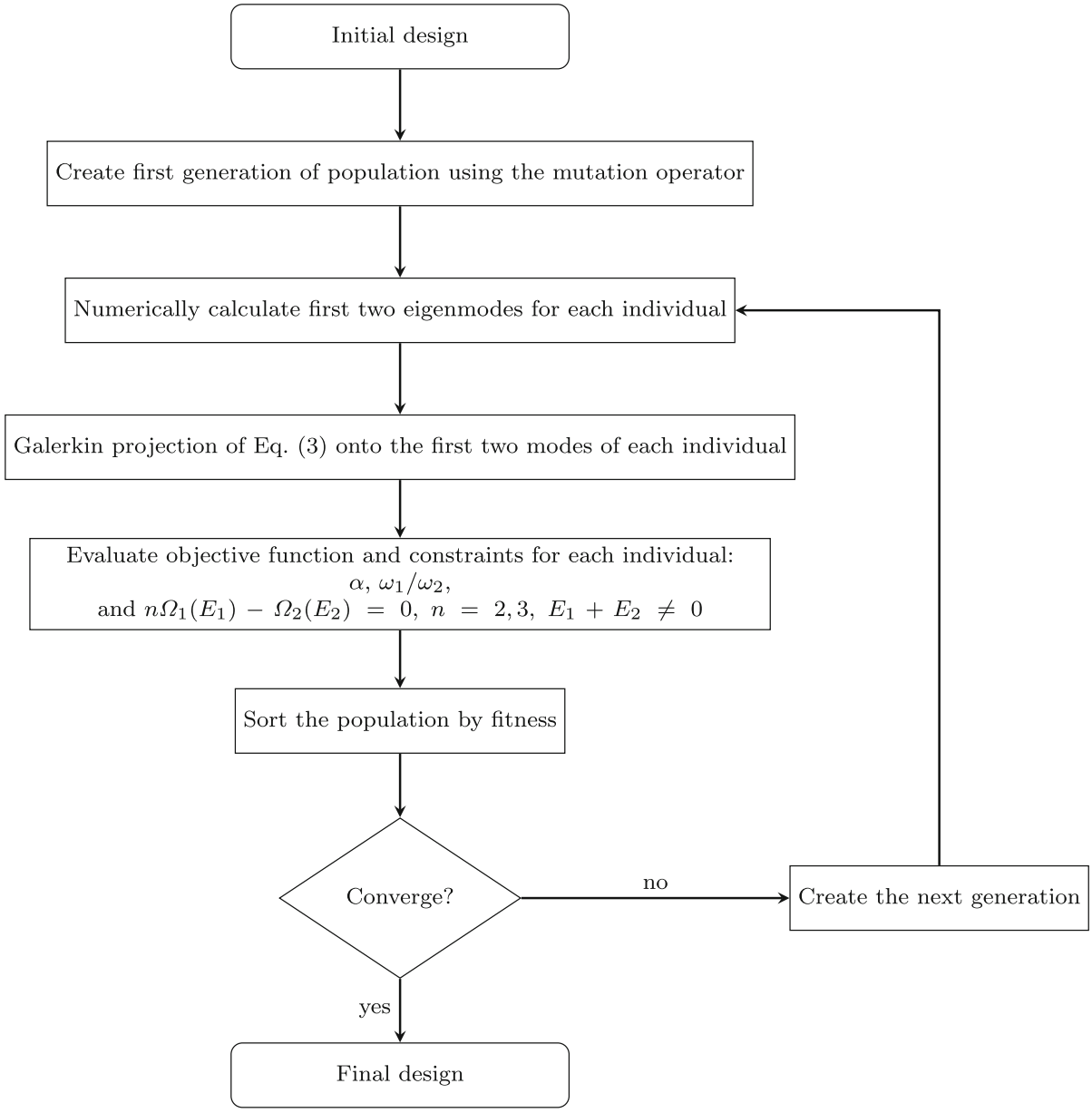

Fig. 4 Flow chart of the shape optimization procedure for enhanced internal resonance using genetic algorithm

erties of silicon, i.e., Young's modulus $\mathcal{E} = 169$GPa and Poisson's ratio $\nu = 0.28$ [69]. Hence, the effective modulus of elasticity (plain strain) is $\mathcal{E}_{\text{eff}} = \mathcal{E}/(1-\nu^2) = 183.377$GPa. The density of silicon is $\rho = 2300\text{kg/m}^3$. Therefore, the transition between the non-dimensional frequency to dimensional frequency is given by $\tilde{\omega} = \omega\sqrt{\mathcal{E}I/\rho A\ell^4} = \omega \cdot 5155.228\text{rad/s}$, and the transition between the non-dimensional energy to dimensional energy is given by $\tilde{E} = E(\mathcal{E}_{\text{eff}} I/\ell) = E_{\text{tot}} \cdot 3.667 \times 10^{-9}\text{J}$.

For both cases of 1-to-2 and 1-to-3 IRs, the genetic algorithm was applied on an initial shape of a straight beam, i.e., $w_0(x) = 0$. The number of grid points (Chebyshev nodes) in each function (and for the rest of the calculations in this paper) is $J + 1 = 101$. The algorithm created a first generation of a popula-

tion of 200 individuals using the mutation operator, and from the second generation, for the case of 1-to-2 IR, the transcendence probability is defined to be 40%, the crossover probability is 25%, and the mutation probability is 35%, which, after multiple runs on every combination of probabilities (for 200 individuals), has given the highest coupling between the modes. For the case of 1-to-3 IR, the probabilities are defined to be 40%, the crossover probability is 20%, and the mutation probability is 40%, which yielded the highest coupling between the modes (see discussion below on sensitivity and multiple solutions of the genetic algorithm). The algorithm converged to an optimal shape function for the case of 1-to-2 IR after 89 generations (Fig. 5), and after 85 generations for the case of 1-to-3 IR (Fig. 6).

We note that our optimization problem is not convex and that multiple local optima could exist. Finding the global optimum of a non-convex optimization is an NP-hard problem, which is out of the scope of our current simple analysis. Furthermore, it is well-known [70–72] that the genetic algorithm is highly sensitive to the procedure in which we evaluate the fitness of a solution and that different procedures can converge to different local optima. Throughout this study, we start the procedure by first satisfying the constraint of nearly rationally related eigenfrequencies $|\omega_1/\omega_2 - 1/n| < \epsilon,\ n = 2, 3,\ \epsilon = 5 \times 10^{-4}$, and therefore, a solution that is closer to IR has a higher fitness value than a solution that has a higher coupling value. After the constraint of nearly rationally related eigenfrequencies was satisfied, we began enhancing the coupling between the modes while satisfying the frequency crossing condition. Moreover, the probability of three operators (transcendence, crossover, and mutation) also plays a significant role in converging the genetic algorithm to a local optimum. In Figs. 7 and 8, we show some of the different values we obtained for the frequency ratio (left panel) and mode coupling (right panel) for different combinations of probabilities. The optimal shape function in each combination converged to an optimal solution within 85 generations for both 1-to-2 and 1-to-3 IRs. The coupling terms obtained for the different combinations ranged between 2.9×10^3 and 2.3×10^5 for the 1-to-2 IR (see Fig. 7) and between 1.8×10^8 to 7.2×10^8 for the 1-to-3 IR (see Fig. 8). We note that while the shape of the optimal curved beam can be considerably different for different probability combinations that yield roughly the same coupling coefficient (Appendix C, Fig. 12), the convergence towards a specific local optimum is robust and only small changes occur (both in the shape of the beam and coupling coefficient) from generation 50 to the final generation 89 (Appendix C, Fig. 13).

To validate that our final designs are prone to the desired IRs, we numerically simulate Eq. (3) with the initial conditions $w(x, 0) = \phi_1(x)q_1(0) + \phi_2(x)q_2(0)$ and $\dot{w}(x, 0) = 0$ as described in subsection 3.3. We project the numerically calculated displacement field $w(x, t)$ onto the first two mode $q_{1,2} = \langle w, \phi_{1,2} \rangle = \int_0^1 w\phi_{1,2}dx$ (Fig. 9). The modal coordinates $q_1(t)$ and $q_2(t)$, clearly show beating types of responses, which correspond to their resonant energy exchange (Fig. 9, bottom). Furthermore, as we show in Appendix C, Fig. 14, the modal interactions also occur when only one of the modes has a non-zero initial energy. The resonant interaction is obvious when the energy is initially only in the first mode as it drives the second mode directly via the term αq_1^n in Eq. (7). However, the second mode drives the first mode parametrically via the term $n\alpha q_1^{n-1} q_2$ in Eq. (6), and hence, when the energy is initially only in the second mode, the resonant interaction occurs due to instability and in the presence of small energy perturbations in the first mode.

The beating envelopes of the modal coordinates can be calculated analytically and compared with the numerical simulations. For the sake of brevity, we show here only the highlights of the analytical calculation of the amplitude modulations for the 1-to-2 IR (see Appendix D for more details). With the inclusion of the dispersive coupling terms, the normal form of the 1-to-2 IR reads

$$\ddot{q_1} + \omega_1^2 q_1 = -\beta_1 q_1^2 - \gamma_1 q_1^3 - 2\alpha q_1 q_2 - 2\eta q_1 q_2^2, \tag{12}$$

$$\ddot{q_2} + \omega_2^2 q_2 = -\beta_2 q_2^2 - \gamma_2 q_2^3 - \alpha q_1^2 - 2\eta q_1^2 q_2. \tag{13}$$

Applying the method of averaging [55], and normalizing the complex amplitude equations as shown in Appendix D, we can describe the action variable I and the angle variable ψ in terms of the averaged Hamiltonian of the system $\mathcal{H}$, the Manly-Rowe invariant $\mathcal{M}$, and the potential of the system $U_{\text{eff}}(I)$.

The potential $U_{\text{eff}}(I)$ is a quartic polynomial in I parameterized by $\mathcal{M}$ and $\mathcal{H}$. It can have a single well or two wells separated by a local maximum [58]. In the case where the local maximum of the double potential

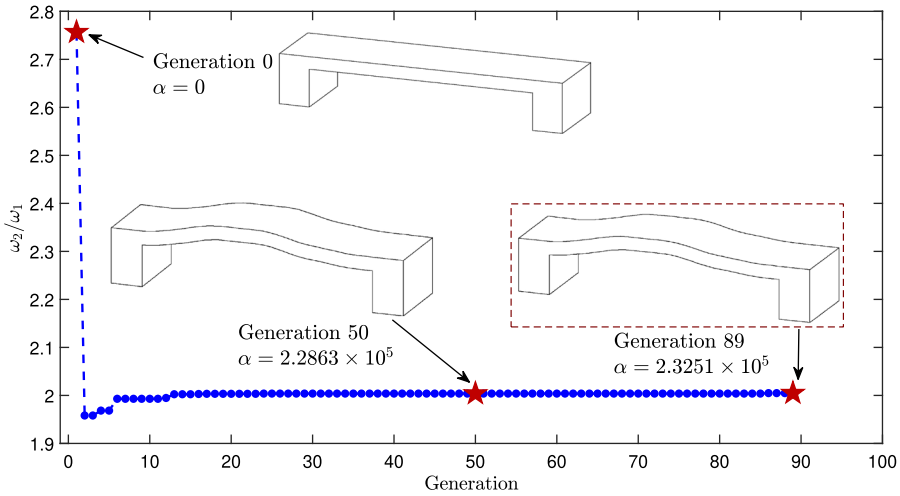

Fig. 5 Shape optimization for 1-to-2 IR. The genetic algorithm evolves the shape of the curved beam and saturates after 89 generations on the final design that optimizes the frequency ratio ω_2/ω_1 and the coupling coefficient while ensuring that the frequency crossing condition of the isolated modes is met

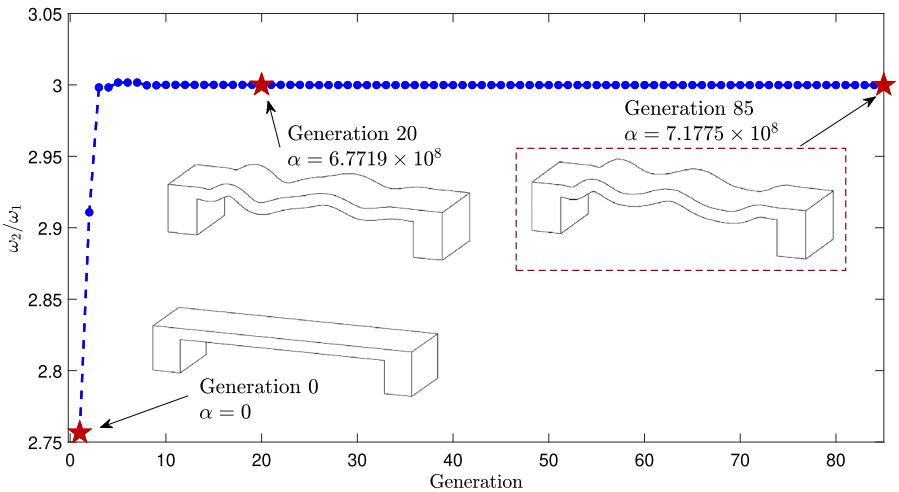

Fig. 6 Shape optimization for 1-to-3 IR. The genetic algorithm evolves the shape of the curved beam and saturates after 85 generations on the final design that optimizes the frequency ratio ω_2/ω_1 and the coupling coefficient while ensuring that the frequency crossing condition of the isolated modes is met

well lies above zero, the equation $U_{\text{eff}}(I) = 0$ has four real solutions $I_1 > I_2 > I_3 > I_4$, where depending on the initial condition $I(0)$, $I(\tau)$ oscillates either between I_1 and I_2, or between I_3 and I_4. In the first case, the oscillations $I(\tau)$ between I_1 and I_2 can be described in terms of Jacobi elliptic functions [73]

$$I(u) = \frac{(I_1 - I_2)I_3\,\mathrm{sn}^2(u|m) - (I_1 - I_3)I_2}{(I_1 - I_2)\,\mathrm{sn}^2(u|m) - (I_1 - I_3)},$$

$$u = \tau\sqrt{\frac{3(48\gamma_1+3\gamma_2-32\eta)^2}{1024\gamma_1^2}}\,\frac{2}{\sqrt{(I_1-I_3)(I_2-I_4)}},$$
$$m = \frac{(I_1 - I_2)(I_3 - I_4)}{(I_1 - I_3)(I_2 - I_4)}. \tag{14}$$

From the above analytical solution, we find that $q_1 = 2\ell_1 I^{1/2}\cos(\omega_1 t + \arg(A_{1n}))$ and $q_2 = 2^{1/2}\ell_2(\mathcal{M} - I)^{1/2}\cos(2\omega_1 t + \arg(A_{2n}))$ (see Appendix D for the definitions of $\ell_{1,2}$ and $A_{1,2n}$). These amplitude mod-

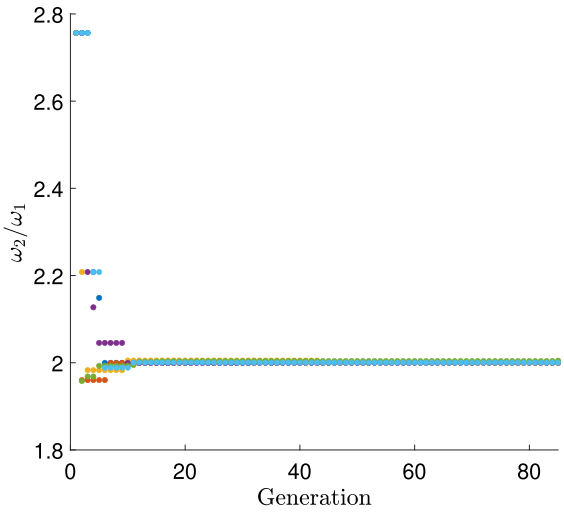

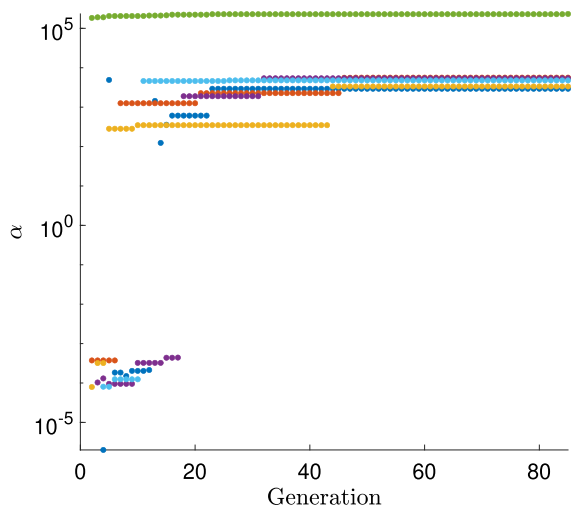

Fig. 7 Convergence to an optimal shape for 1-to-2 IR with different probabilities of the genetic algorithm operators. The ratio of the natural frequencies (left panel) and the mode coupling coefficient (right panel) are shown for different probabilities of {transcendence%, crossover%, mutation%} operators: {20%, 25%, 55%} (blue dots), {20%, 20%, 30%} (orange dots), {25%, 25%, 50%} (yellow dots), {35%, 35%, 30%} (purple dots), {40%, 25%, 35%} (green dots), and {45%, 35%, 20%} (light blue dots). (Color figure online)

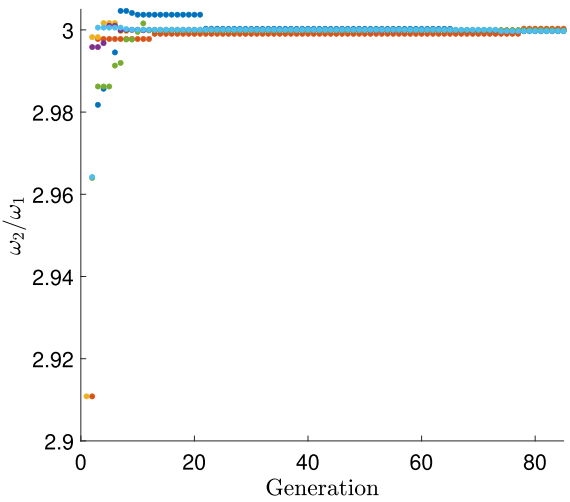

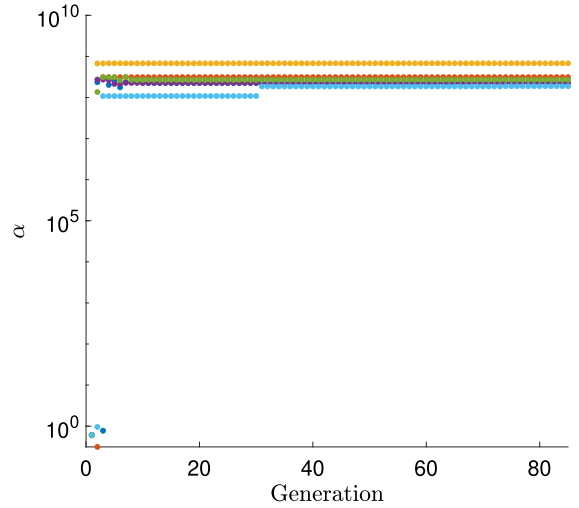

Fig. 8 Convergence to an optimal shape for 1-to-3 IR with different probabilities of the genetic algorithm operators. The ratio of the natural frequencies (left panel) and the mode coupling coefficient (right panel) are shown for different probabilities of {transcendence%, crossover%, mutation%} operators: {20%, 20%, 60%} (blue dots), {20%, 30%, 50%} (orange dots), {40%, 20%, 40%} (yellow dots), {30%, 40%, 30%} (purple dots), {40%, 25%, 35%} (green dots), and {40%, 30%, 30%} (light blue dots). (Color figure online)

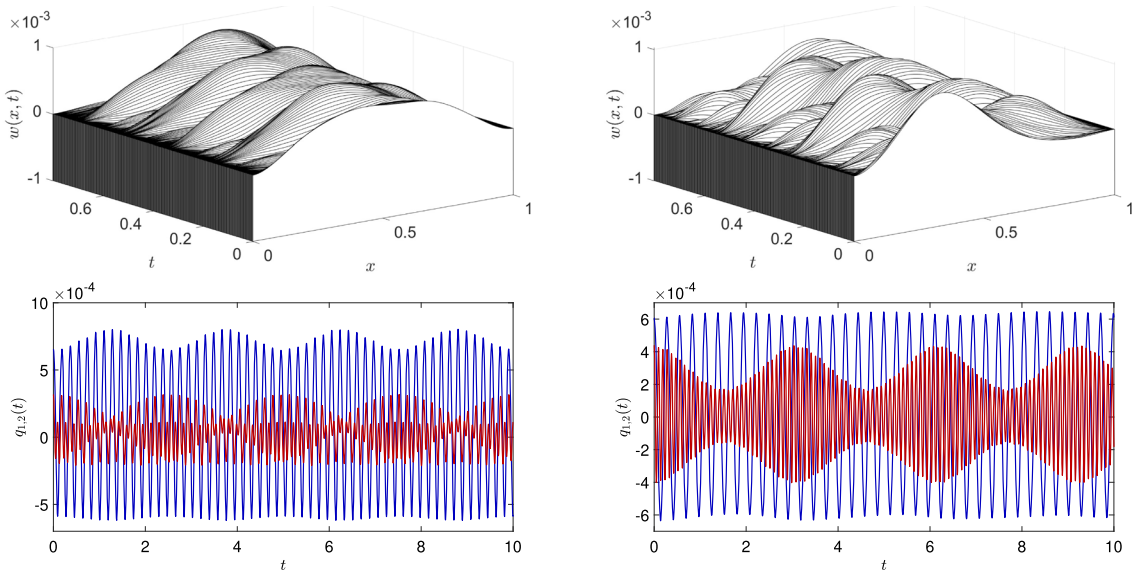

Fig. 9 Numerical simulations of the displacement field $w(x,t)$ for 1-to-2 (left) and 1-to-3 (right) IRs. The nonlinear integro-differential equation of the curved beam [Eq. (3)] is numerically simulated for the final designs of Figs. 5 and 6, and with initial conditions that ensure resonant interaction between the first two modes. The displacement field (upper panels) is projected onto the first two modes of the beam (lower panels). Both 1-to-2 (left) and 1-to-3 (right) IRs, the modulations in the envelope of the first (blue) and the second (red) modes clearly show the energy exchange due to the resonant interaction

ulations of the analytically calculated response are in remarkable agreement with the results from the numerical simulations (Fig. 10). We note that this analytical calculation applies only to conservative systems. However, it can be modified and adjusted to describe the dynamics of high-Q/low-dissipation systems as well [74].

To verify that we used a stable and accurate numerical simulation to solve the partial integro-differential equation [Eq. (3)], we conduct two types of tests:

(i) We compare the power spectra of numerical simulations of the two interacting modes for different time steps. In the left panel of Fig. 11, we show a sample of the power spectrum of the first mode in the vicinity of its eigenfrequency for the 1-to-2 IR beam. Our comparative analysis reveals consistent results across different time-step sizes. Moreover, reducing the time-step size results in slightly narrower peaks and clear sidebands (of spacing $2\omega_b$ around the eigenfrequency) of the amplitude modulations, indicative of improved numerical solution accuracy.

(ii) We evaluate the normalized potential energy of the beam $U/U_{\max}$ after one period $t = T$ for varying time-step sizes. Since all simulations are started from rest conditions, the maximal potential energy is at $t = 0$, i.e., $U(t = 0) = U_{\max}$, and therefore, after one period, the ratio $U/U_{\max}$ should approach closer and closer to unity as we reduce the size of the time step. In the right panel of Fig. 11, we show the "mesh refinement" (convergence to unity with the reduction of time step size) procedure for the 1-to-2 IR beam. As is evident from the figure, the results converge monotonically to unity.

5 Closing remarks

We analyzed and designed curved mechanical beams operating at IR conditions with enhanced coupling between a pair of interacting modes. We numerically calculated the eigenmodes of the curved beams and performed a Galerkin projection to obtain two coupled nonlinear ordinary differential equations for the pair of interacting modal coordinates. After obtaining the modal equations, we formulated an objective function for an optimal design for the curved beam to reach IR with enhanced coupling between the modes. We developed a simple design process using a genetic algorithm

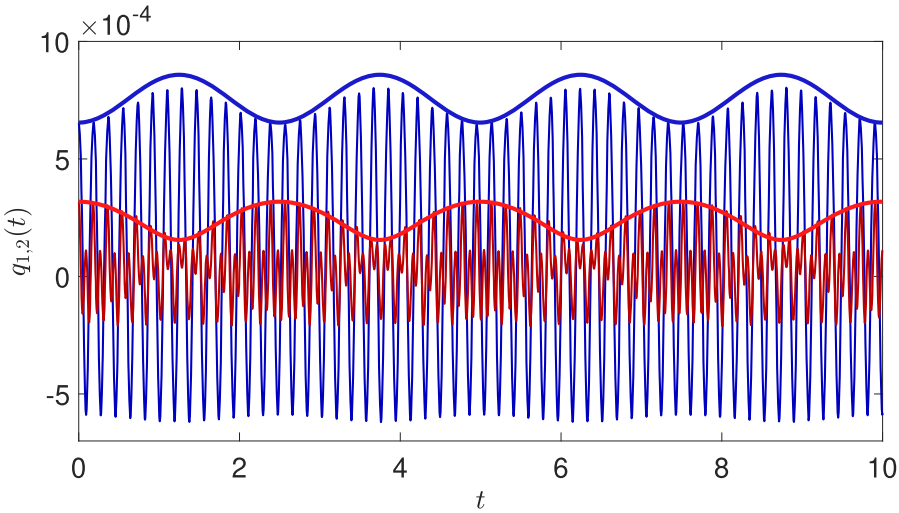

Fig. 10 Comparison between analytical predictions and numerical simulations for 1-to-2 IR. The analytically calculated amplitude modulations (envelope curves) are in excellent agreement with the time evolution of the modal coordinates obtained from the Galerkin projection of the numerically simulated displacement field $w(x, t)$

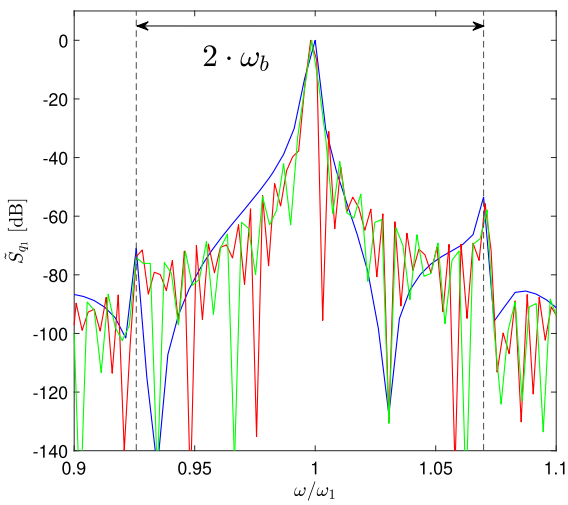

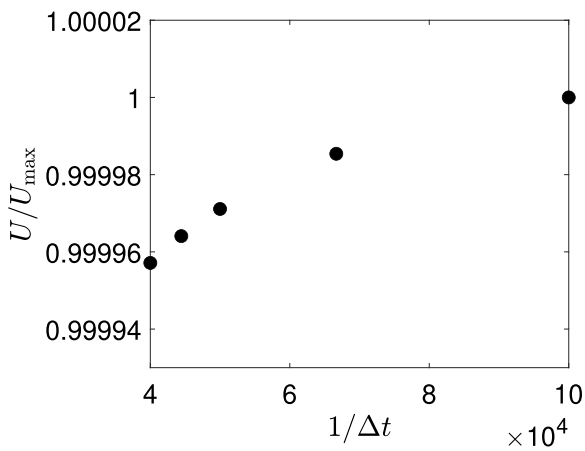

Fig. 11 Numerical stability and accuracy evaluation. Left: The power spectrum of the first mode of the beam in the vicinity of its eigenfrequency for different time-step sizes, $\Delta t = 2 \times 10^{-5}$ (blue), $\Delta t = 1.75 \times 10^{-5}$ (red), and $\Delta t = 1.5 \times 10^{-5}$ (green). Right: The potential energy of 1-to-2 IR beam after one period $t = T$ for different time-step sizes. (Color figure online)

for shape optimization of the curved beam to manipulate the eigenfrequencies and modal coupling via the geometric nonlinearities of the beam.

We provided illustrations for our analysis and design process on the physical properties of MEMS devices for the cases of 1-to-2 and 1-to-3 IRs. We validated that our final designs are prone to the desired IRs using numerical simulations of the partial-integro-differential equation of the beam. Furthermore, we presented the analytical calculations of the resonant envelope modulations for the case of 1-to-2 IR, which showed excellent agreement with the results from the numerical simulations.

In summary, this paper presents a simple tool for intentionally designing enhanced nonlinearity in mechanical beams that promotes a targeted IR. While the presented optimization tool (genetic algorithm) is

extremely simple and perhaps not computationally efficient, it is highly versatile and can optimize various other phenomena of nonlinear dynamics. Moreover, the presented method can also be applied when optimizing a linearized response of a nonlinear system, which is an essentially nonlinear problem, i.e., to what extent the nonlinear effects are negligible. Together with our previous study [53], we present our first steps in a more general quest of embracing nonlinearities and considering them already in the design phase. Such an approach can be highly beneficial and holds great promise for the performance enhancement of MEMS and NEMS devices.

Acknowledgements We would like to thank Steven W. Shaw for critical discussions and invaluable insight that contributed significantly to this work.

Funding S.R. acknowledges the financial support of the Kreitman School of Advanced Graduate Studies at Ben-Gurion University of the Negev under the Negev-Faran Scholarship. YF and OS acknowledge the financial support of the Pearlstone Center of Aeronautical Engineering Studies at Ben-Gurion University of the Negev. YF is also supported by the Israeli Ministry of Infrastructure under Grant No. 222-11-049. OS is also supported by BSF under Grant No. 2018041, and by ISF under Grant No. 344/22.

Data Availability The datasets generated during and/or analyzed during the current study are available from the corresponding author upon reasonable request.

Declarations

Conflict of interest The authors have no relevant financial or non-financial interests to disclose.

Appendix A: Derivation of the nonlinearly coupled ordinary differential equations

Assuming that the motion of the beam is dominated by its first two modes, $w(x,t) = \phi_1(x)q_1(t)+\phi_2(x)q_2(t)$, where $\phi_{1,2}$ are calculated from Eq. (8) and satisfy the orthonormality condition $\langle\phi_k,\phi_l\rangle = \int_0^1 \phi_k\phi_l dx = \delta_{kl}$, we substitute $w(x,t)$ into Eq. (3) and perform Galerkin projection onto $\phi_{1,2}$. This procedure results in the following pair of ordinary differential equations

$$
\begin{aligned}
&\ddot{q}_1 + \omega_1^2 q_1 - 3\chi\left(\int_0^1 \phi_1'^2 dx \int_0^1 \phi_1' w_0' dx\right) q_1^2 - \\
&\quad 2\chi\left(\int_0^1 \phi_1'^2 dx \int_0^1 \phi_2' w_0' dx\right. \\
&\quad \left. +2\int_0^1 \phi_1'\phi_2' dx \int_0^1 \phi_1' w_0' dx\right) q_1 q_2 \\
&\quad -\chi\left(\int_0^1 \phi_2'^2 dx \int_0^1 \phi_1' w_0' dx\right. \\
&\quad \left. +2\int_0^1 \phi_1'\phi_2' dx \int_0^1 \phi_2' w_0' dx\right) q_2^2 \\
&\quad +\chi\left(\int_0^1 \phi_1'^2 dx\right)^2 q_1^3 \\
&\quad +3\chi\left(\int_0^1 \phi_1'^2 dx \int_0^1 \phi_1'\phi_2' dx\right) q_1^2 q_2 \\
&\quad +\chi\left[\int_0^1 \phi_1'^2 dx \int_0^1 \phi_2'^2 dx + 2\left(\int_0^1 \phi_1'\phi_2' dx\right)^2\right] q_1 q_2^2 \\
&\quad +\chi\left(\int_0^1 \phi_2'^2 dx \int_0^1 \phi_1'\phi_2' dx\right) q_2^3 = 0, \qquad (15)
\end{aligned}
$$

$$
\begin{aligned}
&\ddot{q}_2 + \omega_2^2 q_2 - 3\chi\left(\int_0^1 \phi_2'^2 dx \int_0^1 \phi_2' w_0' dx\right) q_2^2 \\
&\quad -2\chi\left(\int_0^1 \phi_2'^2 dx \int_0^1 \phi_1' w_0' dx\right. \\
&\quad \left. +2\int_0^1 \phi_1'\phi_2' dx \int_0^1 \phi_2' w_0' dx\right) q_1 q_2 \\
&\quad -\chi\left(\int_0^1 \phi_1'^2 dx \int_0^1 \phi_2' w_0' dx\right. \\
&\quad \left. +2\int_0^1 \phi_1'\phi_2' dx \int_0^1 \phi_1' w_0' dx\right) q_1^2 \\
&\quad +\chi\left(\int_0^1 \phi_2'^2 dx\right)^2 q_2^3 \\
&\quad +3\chi\left(\int_0^1 \phi_2'^2 dx \int_0^1 \phi_1'\phi_2' dx\right) q_2^2 q_1 \\
&\quad +\chi\left[\int_0^1 \phi_2'^2 dx \int_0^1 \phi_1'^2 dx + 2\left(\int_0^1 \phi_1'\phi_2' dx\right)^2\right] q_2 q_1^2 \\
&\quad +\chi\left(\int_0^1 \phi_1'^2 dx \int_0^1 \phi_1'\phi_2' dx\right) q_1^3 = 0, \qquad (16)
\end{aligned}
$$

which can readily be identified with Eqs. (4)–(5).

Without going into technical details, we outline the derivation of the normal form of the 1-to-2 and 1-to-3 IRs. Since we consider a weakly nonlinear system, Eqs. (4)–(5) can be written as

$$
\begin{aligned}
&\ddot{q}_1 + \omega_1^2 q_1 = \epsilon F_1(q_1, q_2), \\
&\ddot{q}_2 + \omega_2^2 q_2 = \epsilon F_2(q_1, q_2). \qquad (17)
\end{aligned}
$$

As the pair of equations in Eq. (17) are close to those of a pair of linear uncoupled oscillators, we can expect

that their solutions have a nearly sinusoidal (harmonic) form with unknown, and generally time-varying amplitude and phase. Hence, we seek solutions in the following complex form

$$q_1(t) = A_1(t)e^{i\omega_1 t} + c.c.,\ q_2(t) = A_2(t)e^{i\omega_2 t} + c.c., \tag{18}$$

where $c.c.$ denotes the complex conjugate of the preceding term. Note that we make no restriction on $q_{1,2}(t)$ here, as the observed frequencies may well deviate from $\omega_{1,2}$ if the complex–amplitudes $A_{1,2}$ rotate in the complex plane. Introducing a constraint on the time derivative of the two modes, $\dot{q}_n = i\omega_n A_n e^{i\omega_n t} + c.c.,\ n = 1, 2$ (which is dictated by the form of this coordinate change), we find from Eq. (17) the following equations for the complex amplitudes

$$\begin{aligned}\dot{A}_1 &= \epsilon \frac{e^{-i\omega_1 t}}{2i\omega_1} F_1(A_1 e^{i\omega_1 t}, A_2 e^{i\omega_2 t}),\\ \dot{A}_2 &= \epsilon \frac{e^{-i\omega_2 t}}{2i\omega_2} F_2(A_1 e^{i\omega_1 t}, A_2 e^{i\omega_2 t}).\end{aligned} \tag{19}$$

Note that $F_{1,2}$ contain components that are $2\pi/\omega_1$ and $2\pi/\omega_2$ periodic in t. Hence, representing these functions by their corresponding double Fourier series yield

$$\begin{aligned}\dot{A}_1 &= \frac{\epsilon}{2i\omega_1} \sum_{k,l} f_{1_{k,l}} A_1^k e^{i(k-1)\omega_1 t} A_2^l e^{il\omega_2 t},\\ \dot{A}_2 &= \frac{\epsilon}{2i\omega_2} \sum_{q,r} f_{2_{q,r}} A_1^q e^{iq\omega_1 t} A_2^r e^{i(r-1)\omega_2 t},\end{aligned} \tag{20}$$

where $A^{-n} \triangleq \bar{A}^n$ and the over-bar denotes complex-conjugation. Up to this point, the transformations are exact and no approximations have been made.[3] We now use the small parameter ϵ to obtain approximate equations for the evolution of $A_{1,2}$. As the right-hand sides (RHS) of the pair of equations in Eq. (20) are small (of order ϵ in magnitude), the variations of A_1 and A_2 can be either slow (if they are large) or small (if they are fast, e.g., with the frequencies $\omega_1,\ \omega_2$). We restrict ourselves to large and slow variations, i.e., we neglect all the fast and small terms on the RHS of Eq. (20). Neglecting the terms containing the fast oscillations ($e^{in\omega_1 t},\ e^{im\omega_2 t},\ n, m = \pm 1, \pm 2, ...$) can also be considered as an averaging over the period of the oscillations $T_{1,2} = 2\pi/\omega_{1,2}$; thus this method is often called the method of averaging.

From Eq. (20), we see that for a non-zero slowly varying RHS, which implies a resonant interaction between the modes, the fast oscillatory terms, ω_1 and ω_2 must be rationally related, e.g., $\omega_2/\omega_1 = |(k-1)/l|,\ k, l \in \mathbb{Z}$. Note that since k and l can be arbitrary integers, any rationally related frequencies will yield IR. However, due to dissipation, only the lower-order IRs will be observed in practice. For specific values of k and l, we can determine from Eq. (20) the resonant nonlinear coupling terms. The pair $k = -2,\ l = 1$ gives 1-to-3 IR with the lowest-order resonant terms $f_{1_{-2,1}} \bar{A}_1^2 A_2$ and $f_{2_{3,0}} A_1^3$ on the RHS of the first and second equations in Eq. (20), respectively. The pair $k = -1,\ l = 1$ gives 1-to-2 IR with the lowest-order resonant terms $f_{1_{-1,1}} \bar{A}_1 A_2$ and $f_{2_{2,0}} A_1^2$ on the RHS of the first and second equations in Eq. (20), respectively. These terms can be readily associated with the single-term coupling potential $U_{\text{cpl}} = \alpha q_1^n q_2$ that yields Eqs. (6)–(7).

Appendix B: The frequency of oscillation for the isolated modes

Without modal coupling, the equation of motion for the isolated mode can be written as

$$\ddot{q} + U'(q) = 0. \tag{21}$$

where $U = \omega^2 q^2/2 + \beta q^3/3 + \gamma q^4/4$ is the potential energy (per unit mass) of the isolated mode. We multiply Eq. (21) by $\dot{q}$ and integrate with respect to time to obtain the conserved quantity $\dot{q}^2/2 + U(q) = E$, where E is the total energy (per unit mass) of the isolated mode. From the conservation of energy, we find that

$$dt = \pm \frac{dq}{\sqrt{2(E - U(q))}}, \tag{22}$$

where the $\pm$ reflects the change of sign in the velocity $\dot{q}$ when crossing the turning points $q^{(1)}, q^{(2)}$. In half cycle, the resonator starts its motion from the lower turning point $q^{(2)}$ with a positive velocity and arrives

[3] Note that the focus here is only on the resonant coupling terms. Hence, we implicitly disregard the contribution of the resonant terms of each mode that do not stem from the coupling, along with the "dispersive coupling" terms that only shift the frequency of the modes and do not promote modal energy exchange via amplitude modulations. These can, of course, be included as needed.

to the higher turning point $q^{(1)}$. Therefore, we can write

$$\int_0^{\frac{T}{2}} dt = \int_{q^{(2)}}^{q^{(1)}} \frac{dq}{\sqrt{2[E-U(q)]}}. \tag{23}$$

Furthermore, we can rewrite the quadratic polynomial under the square root in the following way

$$\begin{aligned} 2[E-U(q)] &= \frac{\gamma}{4}\left(-q^4 - \frac{4\beta}{3\gamma}q^3 - \frac{2\omega_0^2}{\gamma}q^2 + \frac{4}{\gamma}E\right) \\ &= \frac{\gamma}{4}(q^{(1)}-q)(q-q^{(2)}) \\ &\quad (q-q^{(3)})(q-q^{(4)}). \end{aligned} \tag{24}$$

Thus, from Eq. (23), we find that

$$\frac{T}{2} = \sqrt{\frac{2}{\gamma}} \int_{q^{(2)}}^{q^{(1)}} \frac{dq}{\sqrt{(q^{(1)}-q)(q-q^{(2)})(q-q^{(3)})(q-q^{(4)})}}. \tag{25}$$

We normalize the modal coordinate q by the largest real root $q^{(1)}$, and hence,

$$\frac{T}{2} = \sqrt{\frac{2}{q^{(1)}\gamma}} \int_{q'^{(2)}}^{1} \frac{dq'}{\sqrt{(1-q')(q'-q'^{(2)})(q'-q'^{(3)})(q'-q'^{(4)})}} \tag{26}$$

where $q' = q/q^{(1)}$, $q'^{(1)} = q^{(1)}/q^{(1)} = 1$, $q'^{(2)} = q^{(2)}/q^{(1)}$, $q'^{(3)} = q^{(3)}/q^{(1)}$ and $q'^{(4)} = q^{(4)}/q^{(1)}$. The solution of the elliptic integral in Eq. (26) is given by (cf. Ref. [73], Eq. (259.00))

$$T = 4g'\sqrt{\frac{2}{\gamma}}K(k'), \tag{27}$$

where

$$\begin{aligned} k'^2 &= \frac{1}{4}\frac{(q'^{(1)}-q'^{(2)})^2 - (z'^{(1)}-z'^{(2)})^2}{z'^{(1)}z'^{(2)}}, \\ z'^{(1)^2} &= (q'^{(1)} - \Re\{q'^{(3)}\})^2 + (\Im\{q'^{(3)}\})^2, \\ z'^{(2)^2} &= (q'^{(2)} - \Re\{q'^{(3)}\})^2 + (\Im\{q'^{(3)}\})^2, \\ g' &= \frac{1}{\sqrt{(z'^{(1)}z'^{(2)})}}, \end{aligned} \tag{28}$$

$K(k')$ is an elliptic integral of the first kind, and $\Re\{\cdot\}$ and $\Im\{\cdot\}$ are the real and imaginary parts of $\{\cdot\}$, respectively. Thus, by switching back to the non-normalized variables $q, q^{(1)}, q^{(2)}, q^{(3)}$, and $q^{(4)}$, we find that the fundamental frequency is given by

$$\Omega(E) = \frac{2\pi}{T} = \frac{\pi}{2K(k)}\sqrt{\frac{\gamma}{2}z^{(1)}z^{(2)}}. \tag{29}$$

Appendix C: Supplementary figures

See Figs. 12, 13 and 14

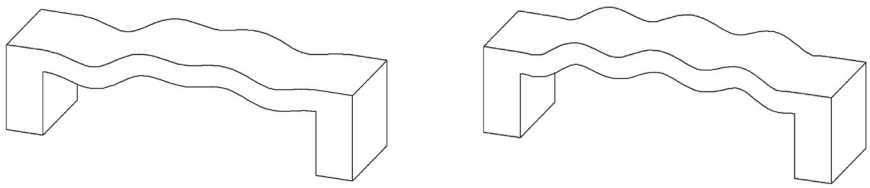

$\alpha = 5.6376 \times 10^3$ $\alpha = 5.7763 \times 10^3$

Fig. 12 Shape functions of the optimal 1-to-2 IR beams that obtained for probabilities combination of {20%, 30%, 50%} (left) and combination of {30%, 40%, 30%} (right)

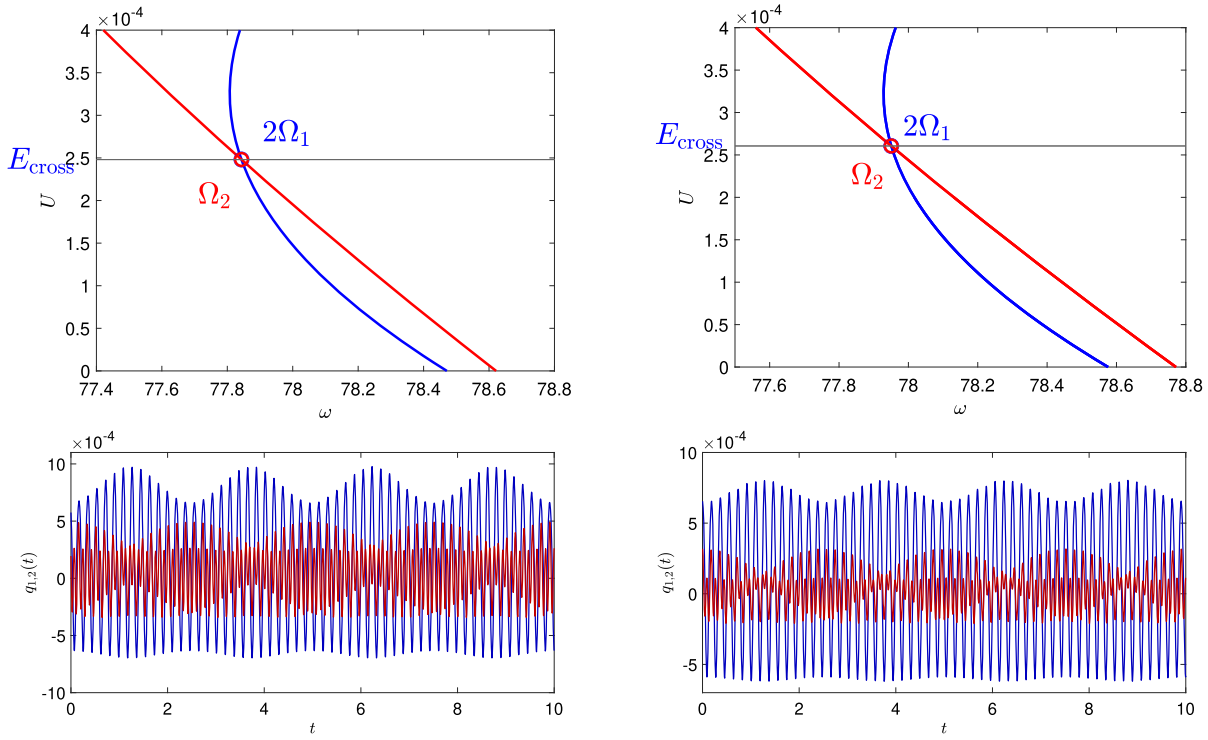

Fig. 13 Comparison between the 1-to-2 IR beam of generation 50 (left) and 1-to-2 IR optimal beam of generation 89 (right). The upper panels are the energy-frequency backbone curves of the first and second modes with the frequency crossing conditions, and the lower panels are the projections of the numerical simulations of the displacement field $w(x, t)$ onto the first two modes of the beam

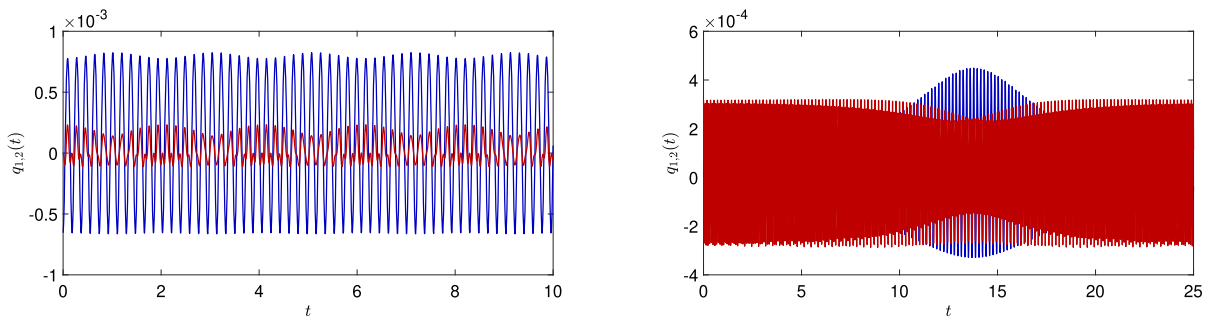

Fig. 14 Projections of the numerical simulations of the displacement field $w(x, t)$ onto the first two modes of the beam for 1-to-2 IR with non-trivial initial conditions in a single mode. Left: the non-trivial initial condition is only on the first mode while the second mode is set to zero initial amplitude. Right: the non-trivial initial condition is only on the second mode while the first mode is set to zero amplitude. The first (blue) and the second (red) modes clearly show the energy exchange due to the resonant interaction for both cases. (Color figure online)

Appendix D: Analytical calculation of resonant envelope modulations

We present here a detailed analysis of the amplitude modulations for the 1-to-2 IR (a similar analysis can be conducted for the 1-to-3, see [58]). By making the ansatz $q_1(t) = A_1(t)e^{i\omega_1 t} + cc$ and $q_2(t) = A_2(t)e^{2i\omega_1 t} + cc$, where cc denotes the complex-conjugate of the preceding term, and applying the method of averaging [55], we obtain from Eqs. (12)–(13) the following pair of complex-amplitude equations

$$\dot{A}_1 = \frac{3i\gamma_1}{2\omega_1}|A_1|^2A_1 + \frac{i\alpha}{\omega_1}A_1^*A_2 + \frac{2i\eta}{\omega_1}A_1|A_2|^2, \quad (30)$$

$$\dot{A}_2 = -i\Delta\omega_2 A_2 + \frac{3i\gamma_2}{4\omega_1}|A_2|^2A_2 + \frac{i\alpha}{4\omega_1}A_1^2 + \frac{i\eta}{\omega_1}|A_1|^2A_2, \quad (31)$$

where $\Delta\omega_2 = 2\omega_1 - \omega_2$ is the frequency mismatch between the modes. We normalize the complex amplitude equations by $\ell_{1,2}A_{1,2n} = A_{1,2}$, where $\ell_1 = 3^{1/4}\omega_1\sqrt{2/\gamma_1}$ and $\ell_2 = 3^{1/4}\omega_1\sqrt{1/\gamma_1}$, the time by $\tau = \omega_1 t$, and obtain the following rescaled equations

$$A_{1n}' = 3\sqrt{3}i|A_{1n}|^2A_{1n} + i\frac{\alpha}{\omega_1}\left(\frac{\sqrt{3}}{\gamma_1}\right)^{\frac{1}{2}}A_{1n}^*A_{2n} + \frac{2\sqrt{3}i\eta}{\gamma_1}A_{1n}|A_{2n}|^2 = -i\frac{\partial\mathcal{H}}{\partial A_{1n}^*}, \quad (32)$$

$$A_{2n}' = -i\Delta\omega_{2n}A_{2n} + \frac{3i\sqrt{3}}{4}\frac{\gamma_2}{\gamma_1}|A_{2n}|^2A_{2n} + i\frac{\alpha}{2\omega_1}\left(\frac{\sqrt{3}}{\gamma_1}\right)^{\frac{1}{2}}A_{1n}^2 + \frac{2\sqrt{3}i\eta}{\gamma_1}|A_{1n}|^2A_{2n}| = -i\frac{\partial\mathcal{H}}{\partial A_{2n}^*}, \quad (33)$$

where $\Delta\omega_{2n} = \Delta\omega_2/\omega_1$, and

$$\mathcal{H} = \Delta\omega_{2n}|A_{2n}|^2 - \frac{3\sqrt{3}}{2}|A_{1n}|^4 - \frac{3\sqrt{3}}{8}\frac{\gamma_2}{\gamma_1}|A_{2n}|^4 - \frac{\alpha}{2\omega_1}\left(\frac{\sqrt{3}}{\gamma_1}\right)^{1/2}\left(A_{1n}^{*\,2}A_{2n} + A_{1n}^2A_{2n}^*\right) - \frac{2\sqrt{3}\eta}{\gamma_1}|A_{1n}|^2|A_{2n}|^2 \quad (34)$$

is the averaged Hamiltonian of the system which, by construction, is a conserved quantity. The second conserved quantity is an analog of the Manly-Rowe invariant that has the form of $\mathcal{M} = I + 2|A_{2n}|^2$, where $I = |A_{1n}|^2$ is the action variable. We define the phase difference $\psi = 2\arg(A_{1n}) - \arg(A_{2n})$ as the angle variable, and rewrite Eqs. (32)–(33) using action-angle variables

$$I' = \frac{\partial\mathcal{H}}{\partial\psi} = \frac{\alpha}{\sqrt{2}\omega_1}\left(\frac{\sqrt{3}}{\gamma_1}\right)^{1/2}(\mathcal{M} - I)^{1/2}I\sin\psi, \quad (35)$$

$$\psi' = -\frac{\partial\mathcal{H}}{\partial I} = \frac{\Delta\omega_{2n}}{2} + 3\sqrt{3}I - \frac{3\sqrt{3}}{16}\frac{\gamma_2}{\gamma_1}(\mathcal{M} - I) + \frac{\alpha}{\sqrt{2}\omega_1}\left(\frac{\sqrt{3}}{\gamma_1}\right)^{1/2}\frac{2\mathcal{M} - 3I}{2(\mathcal{M} - I)^{1/2}}\cos\psi + \frac{\sqrt{3}\eta}{\gamma_1}(\mathcal{M} - 2I). \quad (36)$$

The dynamics of Eqs. (35)–(36) can be mapped onto the motion of a particle trapped in a potential well [58].

$$\frac{1}{2}I'^2 + U_{\text{eff}}(I) = 0,$$

$$U_{\text{eff}}(I) = -\frac{\sqrt{3}\alpha^2}{4\gamma_1\omega_1^2}(\mathcal{M} - I)I^2 + \frac{1}{2}\left[\mathcal{H} - \frac{\Delta\omega_{2n}}{2}(\mathcal{M} - I) + \frac{3\sqrt{3}}{2}I^2 + \frac{3\sqrt{3}}{32}\frac{\gamma_2}{\gamma_1}(\mathcal{M} - I)^2 + \frac{\sqrt{3}\eta}{\gamma_1}I(\mathcal{M} - I)\right]^2. \quad (37)$$

The potential $U_{\text{eff}}(I)$ is a quartic polynomial in I parameterized by $\mathcal{M}$ and $\mathcal{H}$. It can have a single well or two wells separated by a local maximum [58]. In the case where the local maximum of the double potential well lies above zero, the equation $U_{\text{eff}}(I) = 0$ has four real solutions $I_1 > I_2 > I_3 > I_4$, where depending on the initial condition $I(0)$, the "particle trapped in the potential well" $I(\tau)$ oscillates either between I_1 and I_2, or between I_3 and I_4. In the first case, the oscillations $I(\tau)$ between I_1 and I_2 can be described in terms of Jacobi elliptic functions [73]

$$I(u) = \frac{(I_1 - I_2)I_3\,\text{sn}^2(u|m) - (I_1 - I_3)I_2}{(I_1 - I_2)\,\text{sn}^2(u|m) - (I_1 - I_3)},$$

$$u = \tau \sqrt{\frac{3(48\gamma_1 + 3\gamma_2 - 32\eta)^2}{1024\gamma_1^2}} \frac{2}{\sqrt{(I_1 - I_3)(I_2 - I_4)}},$$
$$m = \frac{(I_1 - I_2)(I_3 - I_4)}{(I_1 - I_3)(I_2 - I_4)}. \quad (38)$$

From the above analytical solution, we find that $q_1 = 2\ell_1 I^{1/2} \cos(\omega_1 t + \arg(A_{1n}))$ and $q_2 = 2^{1/2}\ell_2(\mathcal{M} - I)^{1/2} \cos(2\omega_1 t + \arg(A_{2n}))$.

References

1. Strogatz, S.H.: Nonlinear Dynamics and Chaos with Student Solutions Manual: With Applications to Physics, Biology, Chemistry, and Engineering. CRC Press, Boco Raton (2018)
2. Nayfeh, A.H., Balachandran, B.: Applied Nonlinear Dynamics: Analytical, Computational, and Experimental Methods. Wiley, New York (2008)
3. Rosenberg, S., Shoshani, O.: Amplifying the response of a driven resonator via nonlinear interaction with a secondary resonator. Nonlinear Dyn. **105**(2), 1427–1436 (2021). https://doi.org/10.1007/s11071-021-06659-x
4. Antonio, D., Zanette, D.H., López, D.: Frequency stabilization in nonlinear micromechanical oscillators. Nat. Commun. **3**(1), 1–6 (2012)
5. Zhao, C., Sobreviela, G., Pandit, M., Du, S., Zou, X., Seshia, A.: Experimental observation of noise reduction in weakly coupled nonlinear mems resonators. J. Microelectromech. Syst. **26**(6), 1196–1203 (2017)
6. Kozinsky, I., Postma, H.C., Bargatin, I., Roukes, M.: Tuning nonlinearity, dynamic range, and frequency of nanomechanical resonators. Appl. Phys. Lett. **88**(25), 253101 (2006)
7. Shao, L., Palaniapan, M., Tan, W.: The nonlinearity cancellation phenomenon in micromechanical resonators. J. Micromech. Microeng. **18**(6), 065014 (2008)
8. Juillard, J., Bonnoit, A., Avignon, E., Hentz, S., Kacem, N., Colinet, E.: From mems to nems: Closed-loop actuation of resonant beams beyond the critical duffing amplitude. In: SENSORS, 2008 IEEE, pp. 510–513. IEEE (2008)
9. Yurke, B., Greywall, D., Pargellis, A., Busch, P.: Theory of amplifier-noise evasion in an oscillator employing a nonlinear resonator. Phys. Rev. A **51**(5), 4211 (1995)
10. Villanueva, L., Kenig, E., Karabalin, R., Matheny, M., Lifshitz, R., Cross, M., Roukes, M.: Surpassing fundamental limits of oscillators using nonlinear resonators. Phys. Rev. Lett. **110**(17), 177208 (2013)
11. Nitzan, S.H., Zega, V., Li, M., Ahn, C.H., Corigliano, A., Kenny, T.W., Horsley, D.A.: Self-induced parametric amplification arising from nonlinear elastic coupling in a micromechanical resonating disk gyroscope. Sci. Rep. **5**(1), 1–6 (2015)
12. Dou, S., Strachan, B.S., Shaw, S.W., Jensen, J.S.: Structural optimization for nonlinear dynamic response. Philos. Trans. R. Soc. A Math. Phys. Eng. Sci. **373**(2051), 20140,408 (2015)
13. Li, L.L., Polunin, P.M., Dou, S., Shoshani, O., Scott Strachan, B., Jensen, J.S., Shaw, S.W., Turner, K.L.: Tailoring the nonlinear response of mems resonators using shape optimization. Appl. Phys. Lett. **110**(8), 081902 (2017)
14. He, W., Bindel, D., Govindjee, S.: Topology optimization in micromechanical resonator design. Optim. Eng. **13**(2), 271–292 (2012)
15. Rottenberg, X., Jansen, R., Cherman, V., Witvrouw, A., Tilmans, H., Zanaty, M., Khaled, A., Abbas, M.: Metamaterials approach to sensitivity enhancement of mems baw resonant sensors. In: SENSORS, 2013 IEEE, pp. 1–4. IEEE (2013)
16. Li, Y., Luo, W., Zhao, Z., Liu, D.: Resonant excitation-induced nonlinear mode coupling in a microcantilever resonator. Phys. Rev. Appl. **17**(5), 054015 (2022)
17. Li, L., Liu, H., Li, D., Zhang, W.: Theoretical analysis and experiment of multi-modal coupled vibration of piezo-driven π-shaped resonator. Mech. Syst. Signal Process. **192**, 110223 (2023)
18. Zhao, W., Rocha, R.T., Alcheikh, N., Younis, M.I.: Dynamic response amplification of resonant microelectromechanical structures utilizing multi-mode excitation. Mech. Syst. Signal Process. **196**, 110347 (2023)
19. Wang, K., Nguyen, C.C.: High-order medium frequency micromechanical electronic filters. J. Microelectromech. Syst. **8**(4), 534–556 (1999)
20. Lopez, J., Verd, J., Uranga, A., Murillo, G., Giner, J., Marigó, E., Torres, F., Abadal, G., Barniol, N.: Vhf band-pass filter based on a single CMOS-MEMS doubleended tuning fork resonator. Proc. Chem. **1**(1), 1131–1134 (2009)
21. Chi, C.Y., Chen, T.L.: Mems gyroscope control systems for direct angle measurements. In: SENSORS, 2009 IEEE, pp. 492–496. IEEE (2009)
22. Sharma, M., Sarraf, E.H., Baskaran, R., Cretu, E.: Parametric resonance: amplification and damping in mems gyroscopes. Sens. Actuators A **177**, 79–86 (2012)
23. Zhao, C., Montaseri, M.H., Wood, G.S., Pu, S.H., Seshia, A.A., Kraft, M.: A review on coupled mems resonators for sensing applications utilizing mode localization. Sens. Actuators A **249**, 93–111 (2016)
24. Sader, J.E., Hanay, M.S., Neumann, A.P., Roukes, M.L.: Mass spectrometry using nanomechanical systems: beyond the point-mass approximation. Nano Lett. **18**(3), 1608–1614 (2018)
25. Nayfeh, A.H.: Nonlinear Interactions: Analytical, Computational, and Experimental Methods. Wiley, New York (2000)
26. Chen, C., Zanette, D.H., Czaplewski, D.A., Shaw, S., López, D.: Direct observation of coherent energy transfer in nonlinear micromechanical oscillators. Nat. Commun. **8**(1), 1–7 (2017)
27. Yan, Y., Dong, X., Huang, L., Moskovtsev, K., Chan, H.: Energy transfer into period-tripled states in coupled electromechanical modes at internal resonance. Phys. Rev. X **12**(3), 031003 (2022)
28. Wang, M., Perez-Morelo, D.J., Lopez, D., Aksyuk, V.A.: Persistent nonlinear phase-locking and nonmonotonic energy dissipation in micromechanical resonators. Phys. Rev. X **12**(4), 041025 (2022)
29. Czaplewski, D.A., Strachan, S., Shoshani, O., Shaw, S.W., López, D.: Bifurcation diagram and dynamic response of a mems resonator with a 1:3 internal resonance. Appl. Phys. Lett. **114**(25), 254104 (2019)
30. Gobat, G., Zega, V., Fedeli, P., Guerinoni, L., Touzé, C., Frangi, A.: Reduced order modelling and experimental val-

idation of a mems gyroscope test-structure exhibiting 1:2 internal resonance. Sci. Rep. **11**(1), 16,390 (2021)
31. Eriksson, A.M., Shoshani, O., López, D., Shaw, S.W., Czaplewski, D.A.: Controllable branching of robust response patterns in nonlinear mechanical resonators. Nat. Commun. **14**(1), 161 (2023)
32. Gobat, G., Zega, V., Fedeli, P., Touzé, C., Frangi, A.: Frequency combs in a mems resonator featuring 1:2 internal resonance: ab initio reduced order modelling and experimental validation. Nonlinear Dyn. **111**(4), 2991–3017 (2023)
33. Miles, J.W.: Stability of forced oscillations of a spherical pendulum. Q. Appl. Math. **20**, 21–32 (1962)
34. Miles, J.: Resonant motion of a spherical pendulum. Phys. D **11**(3), 309–323 (1984)
35. Johnson, J., Bajaj, A.K.: Amplitude modulated and chaotic dynamics in resonant motion of strings. J. Sound Vib. **128**(1), 87–107 (1989)
36. Sethna, P.: Vibrations of dynamical systems with quadratic nonlinearities. J. Appl. Mech. **32**(3), 576–582 (1965)
37. Haddow, A., Barr, A., Mook, D.: Theoretical and experimental study of modal interaction in a two-degree-of-freedom structure. J. Sound Vib. **97**(3), 451–473 (1984)
38. Chin, C.M., Nayfeh, A.H.: Three-to-one internal resonances in hinged-clamped beams. Nonlinear Dyn. **12**(2), 129–154 (1997)
39. Chin, C.M., Nayfeh, A.H.: Three-to-one internal resonances in parametrically excited hinged-clamped beams. Nonlinear Dyn. **20**(2), 131–158 (1999)
40. Tondl, A.: Autoparametric Resonance in Mechanical Systems. Cambridge University Press, Cambridge (2000)
41. Czaplewski, D.A., Chen, C., Lopez, D., Shoshani, O., Eriksson, A.M., Strachan, S., Shaw, S.W.: Bifurcation generated mechanical frequency comb. Phys. Rev. Lett. **121**(24), 244302 (2018)
42. Gobat, G., Guillot, L., Frangi, A., Cochelin, B., Touzé, C.: Backbone curves, Neimark-sacker boundaries and appearance of quasi-periodicity in nonlinear oscillators: application to 1: 2 internal resonance and frequency combs in mems. Meccanica **56**(8), 1937–1969 (2021)
43. Keşkekler, A., Shoshani, O., Lee, M., van der Zant, H.S., Steeneken, P.G., Alijani, F.: Tuning nonlinear damping in graphene nanoresonators by parametric-direct internal resonance. Nat. Commun. **12**(1), 1099 (2021)
44. Güttinger, J., Noury, A., Weber, P., Eriksson, A.M., Lagoin, C., Moser, J., Eichler, C., Wallraff, A., Isacsson, A., Bachtold, A.: Energy-dependent path of dissipation in nanomechanical resonators. Nat. Nanotechnol. **12**(7), 631–636 (2017)
45. Aravindan, M., Ali, S.F.: Exploring 1:3 internal resonance for broadband piezoelectric energy harvesting. Mech. Syst. Signal Process. **153**, 107493 (2021)
46. Fan, Y., Ghayesh, M.H., Lu, T.F.: High-efficient internal resonance energy harvesting: modelling and experimental study. Mech. Syst. Signal Process. **180**, 109402 (2022)
47. Mathew, J.P., Patel, R.N., Borah, A., Vijay, R., Deshmukh, M.M.: Dynamical strong coupling and parametric amplification of mechanical modes of graphene drums. Nat. Nanotechnol. **11**(9), 747–751 (2016)
48. Keskekler, A., Arjmandi-Tash, H., Steeneken, P.G., Alijani, F.: Symmetry-breaking-induced frequency combs in graphene resonators. Nano Lett. **22**(15), 6048–6054 (2022)
49. Ouakad, H.M., Younis, M.I., Alsaleem, F.M., Miles, R., Cui, W.: The static and dynamic behavior of mems arches under electrostatic actuation. In: International Design Engineering Technical Conferences and Computers and Information in Engineering Conference, vol. 49033, pp. 607–616 (2009)
50. Krylov, S., Dick, N.: Dynamic stability of electrostatically actuated initially curved shallow micro beams. Contin. Mech. Thermodyn. **22**(6–8), 445–468 (2010)
51. Medina, L., Gilat, R., Krylov, S.: Dynamic release condition in latched curved micro beams. Commun. Nonlinear Sci. Numer. Simul. **73**, 291–306 (2019)
52. Hajjaj, A.Z., Younis, M.I.: Theoretical and experimental investigation of two-to-one internal resonance in MEMS arch resonators. J. Comput. Nonlinear Dyn. **14**(011), 001–1 (2019)
53. Rosenberg, S., Shoshani, O.: Zero-dispersion point in curved micro-mechanical beams. Nonlinear Dyn. **107**, 1–14 (2022)
54. Touzé, C., Thomas, O., Chaigne, A.: Hardening/softening behaviour in non-linear oscillations of structural systems using non-linear normal modes. J. Sound Vib. **273**(1–2), 77–101 (2004)
55. Guckenheimer, J., Holmes, P.: Nonlinear Oscillations, Dynamical Systems, and Bifurcations of Vector Fields, vol. 42. Springer, Cham (2013)
56. Touzé, C.: Normal form theory and nonlinear normal modes: theoretical settings and applications. In: Modal Analysis of Nonlinear Mechanical Systems, pp. 75–160. Springer, Cham (2014)
57. Shami, Z.A., Shen, Y., Giraud-Audine, C., Touzé, C., Thomas, O.: Nonlinear dynamics of coupled oscillators in 1:2 internal resonance: effects of the non-resonant quadratic terms and recovery of the saturation effect. Meccanica **57**(11), 2701–2731 (2022)
58. Shoshani, O., Shaw, S.W.: Resonant modal interactions in micro/nano-mechanical structures. Nonlinear Dyn. **104**, 1801–1828 (2021)
59. Woon, S.Y., Querin, O.M., Steven, G.P.: Structural application of a shape optimization method based on a genetic algorithm. Struct. Multidiscip. Optim. **22**, 57–64 (2001)
60. Boyd, J.P.: Chebyshev and Fourier spectral methods. Courier Corporation, Chelmsford (2001)
61. Trefethen, L.N.: Spectral methods in MATLAB. SIAM (2000)
62. Yagci, B., Filiz, S., Romero, L.L., Ozdoganlar, O.B.: A spectral-tchebychev technique for solving linear and nonlinear beam equations. J. Sound Vib. **321**(1–2), 375–404 (2009)
63. Frank, W., von Brentano, P.: Classical analogy to quantum mechanical level repulsion. Am. J. Phys. **62**(8), 706–709 (1994)
64. Novotny, L.: Strong coupling, energy splitting, and level crossings: a classical perspective. Am. J. Phys. **78**(11), 1199–1202 (2010)
65. Abramowitz, M., Stegun, I.A.: Handbook of mathematical functions with formulas, graphs, and mathematical table. In: US Department of Commerce. National Bureau of Standards Applied Mathematics series 55 (1965)
66. Younis, M.I.: MEMS Linear and Nonlinear Statics and Dynamics, vol. 20. Springer, Cham (2011)
67. Shaw, S.W., Rosenberg, S., Shoshani, O.: A hybrid averaging and harmonic balance method for weakly nonlinear

asymmetric resonators. Nonlinear Dyn. **111**(5), 3969–3979 (2023)
68. Abramowitz, M., Stegun, I.A.: Handbook of Mathematical Functions with Formulas, Graphs, and Mathematical Tables, vol. 55. US Government printing office (1968)
69. Hopcroft, M.A., Nix, W.D., Kenny, T.W.: What is the young's modulus of silicon? J. Microelectromech. Syst. **19**(2), 229–238 (2010)
70. Kramer, O., Kramer, O.: Genetic Algorithms. Springer, Cham (2017)
71. Mirjalili, S., Mirjalili, S.: Genetic algorithm. In: Evolutionary Algorithms and Neural Networks: Theory and Applications, pp. 43–55. Springer, Cham (2019)
72. Katoch, S., Chauhan, S.S., Kumar, V.: A review on genetic algorithm: past, present, and future. Multimed. Tools Appl. **80**, 8091–8126 (2021)
73. Byrd, P.F., Friedman, M.D.: Handbook of Elliptic Integrals for Engineers and Physicists, vol. 67. Springer, Cham (2013)
74. Shoshani, O., Shaw, S.W., Dykman, M.I.: Anomalous decay of nanomechanical modes going through nonlinear resonance. Sci. Rep. **7**(1), 18091 (2017)